Dihydrofolate reductase activity controls neurogenic transitions in the developing neocortex

Sulov Saha, Thomas Jungas, David Ohayon, Christophe Audouard, Tao Ye, Mohamad-Ali Fawal, Alice Davy

© 2023. Published by The Company of Biologists Ltd | Development (2023) 150, dev201696. doi:10.1242/dev.201696

RESEARCH ARTICLE

Dihydrofolate reductase activity controls neurogenic transitions in the developing neocortex

Sulov Saha[1], Thomas Jungas[1], David Ohayon[1], Christophe Audouard[1], Tao Ye[2], Mohamad-Ali Fawal[1] and Alice Davy[1,*]

ABSTRACT

One-carbon/folate (1C) metabolism supplies methyl groups required for DNA and histone methylation, and is involved in the maintenance of self-renewal in stem cells. Dihydrofolate reductase (DHFR), a key enzyme in 1C metabolism, is highly expressed in human and mouse neural progenitors at the early stages of neocortical development. Here, we have investigated the role of DHFR in the developing neocortex and report that reducing its activity in human neural organoids and mouse embryonic neocortex accelerates indirect neurogenesis, thereby affecting neuronal composition of the neocortex. Furthermore, we show that decreasing DHFR activity in neural progenitors leads to a reduction in one-carbon/folate metabolites and correlates with modifications of H3K4me3 levels. Our findings reveal an unanticipated role for DHFR in controlling specific steps of neocortex development and indicate that variations in 1C metabolic cues impact cell fate transitions.

KEY WORDS: One-carbon metabolism, Neocortex, Neural progenitors, Organoids, Mouse genetics

INTRODUCTION

One-carbon (1C) metabolism is a universal metabolic process composed of two intertwined cycles, the folate cycle and the methionine cycle, that collectively sustain the biosynthesis of purine, thymidine and methyl groups (Clare et al., 2018; Ducker and Rabinowitz, 2017). As such, 1C metabolism is necessary for DNA replication as well as protein and DNA methylation. Although the folate cycle has been extensively studied for its role in cell proliferation, recent studies revealed a role for the methionine cycle in self-renewal of stem cells through the regulation of histone methylation (Fawal et al., 2018, 2021; Shiraki et al., 2014; Shyh-Chang et al., 2013). Specifically, it has been shown that perturbation of the methionine cycle leads to a decrease in H3K4 trimethylation, which in turn impacts gene expression (Fawal et al., 2018; Mentch et al., 2015; Shiraki et al., 2014; Shyh-Chang et al., 2013). Dihydrofolate reductase (DHFR), an enzyme positioned upstream of the two cycles, is crucial for converting dietary folate into tetrahydrofolate (THF), and its downstream folate species are required for both DNA synthesis and methylation reactions. *DHFR* is classified as a housekeeping gene expressed in all cycling cells whose expression varies proportionally to cell growth (Feder et al., 1989). Yet human genetic studies showed that DHFR deficiency leads to hematological and neurological phenotypes in humans (Banka et al., 2011; Cario et al., 2011), indicating that DHFR has tissue-specific functions. Furthermore, a recent single-cell gene expression analysis revealed that *DHFR* mRNA is dynamically expressed in human and mouse neural progenitors over the course of neocortex development (Klingler et al., 2021), suggesting that it could play specific roles in this developmental process.

The mammalian neocortex develops according to an ordered temporal sequence that begins with the amplification of neuroepithelial cells, which are the founder stem cell population. After an active phase of proliferation, neuroepithelial cells transition into apical progenitors that are anchored to both the apical and basal side of the cortical wall, with their cell bodies forming the ventricular zone (VZ) (Noctor et al., 2001; Rakic, 1972). These apical progenitors express the transcription factor PAX6 (Götz et al., 1998) and give rise to glutamatergic projection neurons populating the six layers of the neocortex, numbered I to VI, in a sequential 'inside-out' manner (except for early-born uppermost layer I neurons). In the mouse neocortex, at the onset of neurogenesis, a fraction of $PAX6^+$ apical progenitors generate early-born deep layer (V-VI) neurons by direct neurogenesis (Cárdenas et al., 2018). During the mid-late stages of neurogenesis, $PAX6^+$ apical progenitors generate neurons mostly by indirect neurogenesis, which involves the production of intermediate progenitors expressing the transcription factor TBR2 (Haubensak et al., 2004; Miyata et al., 2004; Noctor et al., 2004; Sessa et al., 2008). Although $TBR2^+$ intermediate progenitors in the subventricular zone (SVZ) symmetrically divide to generate neurons of all layers, at later stages they mainly give rise to late born upper layer (II-IV) neurons (Vasistha et al., 2015). In humans, the number of $TBR2^+$ progenitors and other types of intermediate progenitors is massively expanded (Hansen et al., 2010) and neurogenesis is mostly indirect, although evidence of direct neurogenesis at early developmental stages has been reported for the production of deep layer neurons (Eze et al., 2021). Newborn neurons subsequently migrate radially towards the cortical plate (CP) and express specific factors that control their final positioning and axonal targeting to establish circuit connections, such as TBR1 for layer VI neurons, CTIP2 for layer V neurons or SATB2 for layer II-IV neurons (Molyneaux et al., 2007).

Here, to address whether DHFR plays a role in specific steps of neocortex development, we reduced DHFR activity both in mouse and human models, with, respectively, *in vivo* and *in vitro* approaches. First, we generated haploinsufficient $Dhfr^{+/\Delta}$ mice and observed a loss of $CTIP2^+$ early-born neurons associated with

[1]Molecular, Cellular and Developmental Biology Unit (MCD), Centre de Biologie Intégrative (CBI), Université de Toulouse, CNRS, UPS, 118 route de Narbonne, 31062 Toulouse, France. [2]Institut de Génétique et de Biologie Moléculaire et Cellulaire (IGBMC), INSERM U1258, CNRS UMR7104, Université de Strasbourg, 1 rue Laurent Fries, 67404 Illkirch, France.

*Author for correspondence (alice.davy@univ-tlse3.fr)

A.D., 0000-0003-2134-4526

Handling Editor: Lydia Finley
Received 11 February 2023; Accepted 1 August 2023

Development (2023) 150, dev201696. doi:10.1242/dev.201696

an increase in TBR2$^+$ intermediate progenitors and SATB2$^+$ late-born neurons. Second, we report that DHFR pharmacological inhibition at an early stage of human neural organoid (HNO) development leads to a depletion in PAX6$^+$ apical progenitors and overproduction of TBR2$^+$ intermediate progenitors resulting in accelerated generation of CTIP2$^+$ early-born neurons and SATB2$^+$ late-born neurons. Both findings suggest that DHFR deficiency prematurely initiates indirect neurogenesis and has a functional impact on the generation of neuron subtypes. Mechanistically, we find that these changes in neuronal subtype generation correlate with decreased steady-state levels of THF and S-adenosyl methionine (SAM) metabolites and with a global decrease in H3K4 trimethylation (H3K4me3) marks. Genome-wide analyses revealed changes in this histone methylation mark at genes that are specific to neuronal subtypes.

RESULTS

DHFR haploinsufficient embryos exhibit early neocortex developmental delay

DHFR is classified as a housekeeping enzyme, yet data mining shows that *Dhfr* mRNA is expressed dynamically in the developing mouse neocortex, with a high expression in PAX6$^+$ apical progenitors at early stages of development and a low expression in TBR2$^+$ progenitors and in neurons (Fig. 1A, Fig. S1A,B) (Di Bella et al., 2021; Telley et al., 2019; Visel et al., 2004). By using western blot analyses, we confirmed that expression of DHFR protein is highest at E12.5 in the developing mouse head (Fig. 1B). To investigate the role of DHFR on neurogenesis *in vivo* and the long-term consequences of its inhibition on neocortex development, we generated a *Dhfr* mutant mouse line by deleting exon 5 of the *Dhfr* gene, which harbors the catalytic activity (Fig. 1C). Genotyping of E4.5 embryos revealed a wild-type and a deleted allele, indicating that genome editing was successful (Fig. S1C); RT-PCR and qRT-PCR analyses on wild-type and *Dhfr*$^{+/\Delta}$ heterozygous E12.5 embryos showed that the deleted allele was transcribed (Fig. S1D,E). In tissue extracts from E12.5 embryos, DHFR protein levels were halved in *Dhfr*$^{+/\Delta}$ samples compared with wild type (Fig. 1D) and a similar decrease in DHFR activity was observed in *Dhfr*$^{+/\Delta}$ samples compared with wild type (Fig. 1E). Despite this decreased DHFR activity, *Dhfr*$^{+/\Delta}$ heterozygous mutants were viable and fertile with normal body weight (Fig. S1F).

To gain insight into the role of DHFR in early neocortex development, we assessed progenitor and neuron populations in the *Dhfr*$^{+/\Delta}$ heterozygous mutants at E12.5. This revealed that the number of PAX6$^+$ apical progenitors was reduced in the lateral neocortex of *Dhfr*$^{+/\Delta}$ embryos compared with wild-type embryos, with no change in TBR2$^+$ intermediate progenitors (Fig. 1F,G). In addition, we used TBR1, a marker of immature neurons (predominantly layer VI), CTIP2 (a marker of layer V neurons) and SATB2 (predominantly layer II-IV) to quantify the production of projection neuron subtypes. In the lateral neocortex of E12.5 *Dhfr*$^{+/\Delta}$ embryos, the number of TBR1$^+$ neurons was not significantly changed, the number of CTIP2$^+$ neurons was decreased while no SATB2$^+$ neurons could be detected in either genotype (Fig. 1H-J). DHFR plays a well-known function in cell proliferation; we thus expected that the origin of the decrease in progenitors and CTIP2$^+$ neurons was due to decreased proliferation. However, we observed no significant differences in phospho-histone H3 (pH3)-positive cells at the VZ of *Dhfr*$^{+/\Delta}$ embryos compared with wild type (Fig. S2A,B), suggesting unchanged proliferation rate of apical progenitors. In addition, immunostaining for the apoptotic marker cleaved caspase 3 (CASP3) detected only a few condensed nuclei or CASP3-positive cells in wild-type and *Dhfr*$^{+/\Delta}$ neocortex (Fig. S2C,D), indicating that the decrease in progenitor and neuron populations is not due to cell death. Next, we performed bulk RNA-sequencing at E12.5, comparing wild-type and *Dhfr*$^{+/\Delta}$ embryonic neocortex. PCA analyses with the entire gene set showed that the samples could be partly clustered by genotypes (Fig. 1K). However, a PCA bi-plot analysis using a subset of 258 genes specific for E12.5 neocortex (Di Bella et al., 2021) revealed an association of the majority of these genes with wild-type samples (Fig. 1L), suggesting that the main difference in expression profiles between genotypes is related to genes that define this embryonic stage. Further bioinformatics analyses identified about 250 genes that are differentially expressed in *Dhfr*$^{+/\Delta}$ embryonic neocortex (Fig. S2E), and we confirmed the molecular signature of an immature brain with decreased expression of *Ttr* and *Aldoc* by qRT-PCR in *Dhfr*$^{+/\Delta}$ embryos (Fig. S2F). Altogether, these results reveal a delayed progression of early neocortical development in *Dhfr*$^{+/\Delta}$ embryos.

DHFR deficiency promotes indirect neurogenesis in the mouse neocortex

No significant difference in cortical thickness was observed between wild-type and *Dhfr*$^{+/\Delta}$ heterozygous embryos (Fig. S3A,B), indicating that, despite an initial developmental delay, the general growth of the neocortex is not impaired in *Dhfr*$^{+/\Delta}$ mutant embryos. To investigate the consequences of reduced DHFR activity on neurogenesis at later stages of mouse neocortex development, we quantified progenitor and neuron populations at E14.5 in wild-type and *Dhfr*$^{+/\Delta}$ embryos. Although the number of PAX6$^+$ apical progenitors was unchanged, the number of TBR2$^+$ intermediate progenitors was increased in E14.5 *Dhfr*$^{+/\Delta}$ lateral neocortex (Fig. 2A,B), suggesting that TBR2$^+$ intermediate progenitors were produced at a higher rate from PAX6$^+$ apical progenitors between E12.5 and E14.5. The number of pH3-positive cells within the SVZ was increased (Fig. 2C,D), corresponding to the increased abundance of TBR2$^+$ intermediate progenitors. In terms of neurons, the number of TBR1$^+$ neurons was unchanged in lateral neocortex, but the number of CTIP2$^+$ neurons was decreased while the number of SATB2$^+$ neurons was strongly increased (Fig. 2E-G), indicating a potential switch between direct neurogenesis (generating CTIP2$^+$ neurons) and indirect neurogenesis (generating SATB2$^+$ neurons from TBR2$^+$ progenitors). To test for this hypothesis, we injected EdU (5 mg/ml) at E12.5 and monitored the fate of EdU$^+$ cells at E14.5. In *Dhfr*$^{+/\Delta}$ embryos, the fraction of EdU$^+$/TBR2$^+$ cells and EdU$^+$/SATB2$^+$ was increased whereas the fraction of EdU$^+$/CTIP2$^+$ cells was decreased compared with wild type (Fig. 2H-J). These data indicate that progenitors that were cycling at E12.5 generated more TBR2$^+$ progenitors at the expense of CTIP2$^+$ neurons, thus supporting the notion of a precocious switch from direct to indirect neurogenesis in *Dhfr*$^{+/\Delta}$ mutants.

At E16.5, the number of PAX6$^+$ progenitors is indistinguishable between wild-type and *Dhfr*$^{+/\Delta}$ neocortex whereas the number of TBR2$^+$ progenitors is decreased (Fig. 3A,B), possibly reflecting an accelerated neurogenesis. The imbalance in neuronal composition persists with fewer CTIP2$^+$ and an excess of SATB2$^+$ neurons in *Dhfr*$^{+/\Delta}$ neocortex compared with wild type at E16.5 (Fig. 3C-F). This persisting change of neuronal fate in *Dhfr*$^{+/\Delta}$ neocortex was confirmed at E19.5/P0 using CTIP2 and SATB2 as well as CUX1, which is a marker of late-born, upper layer neurons (Fig. 3G,H). Noticeably, this altered neuronal composition was still observed in *Dhfr*$^{+/\Delta}$ somatosensory neocortex at postnatal P21 stage (Fig. S3C,D), with a decreased number of CTIP2$^+$ neurons and an increased number of SATB2$^+$ neurons, revealing long-term changes in neuronal

Development (2023) 150, dev201696. doi:10.1242/dev.201696

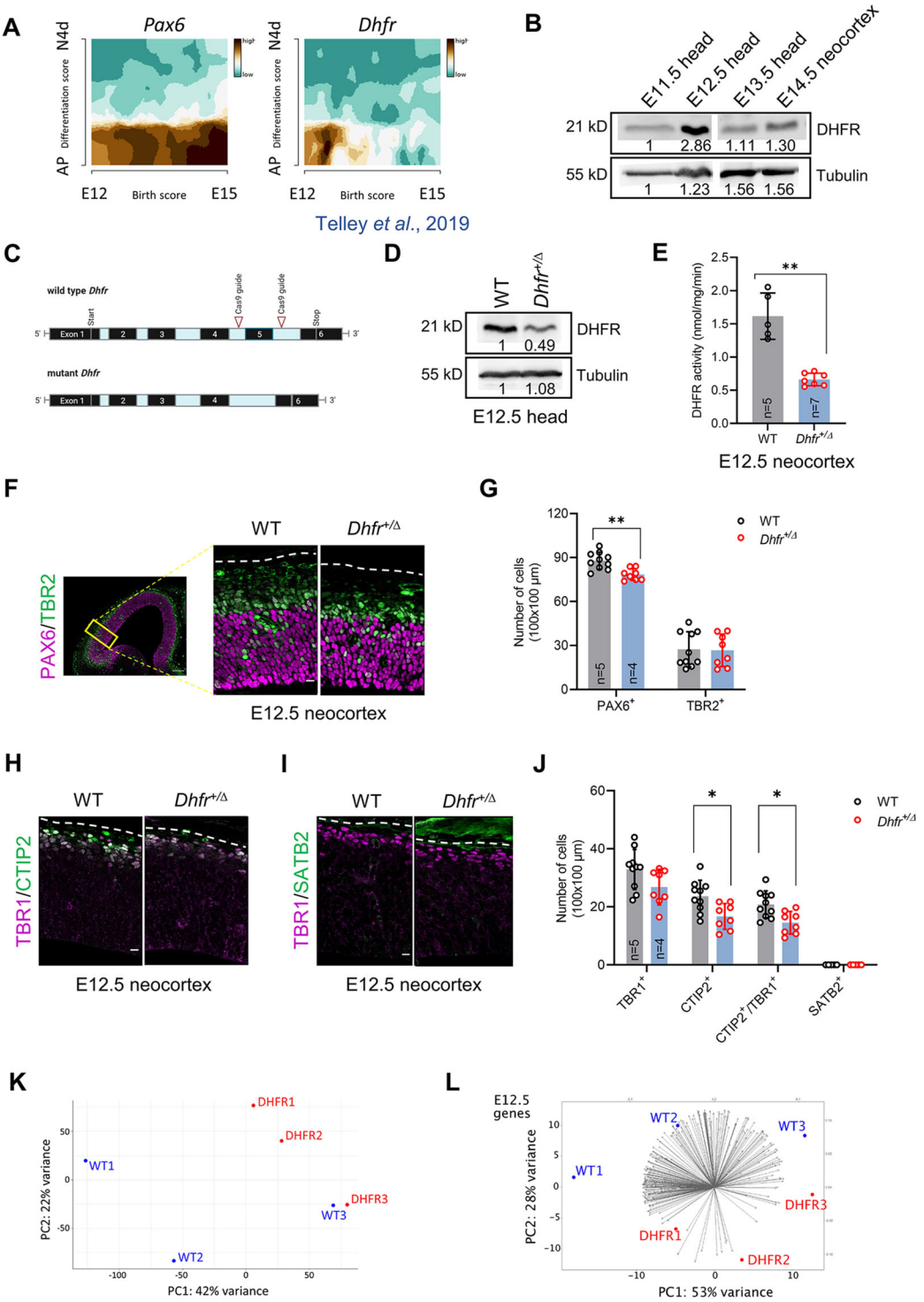

Fig. 1. *Dhfr* heterozygous mutant mice exhibits early neurodevelopmental delay. (A) *Dhfr* mRNA expression in the developing mouse neocortex (data collected from http://genebrowser.unige.ch/telagirdon/). AP, apical progenitors; E, embryonic day; N4d, 4-day-old neurons. (B) Western blot analysis of wild-type tissue extracts at different developmental stages (n=2). Primary antibodies are indicated on the right. Tubulin was used as a loading control. Numbers indicate relative levels over time. (C) Schematic representation of the wild-type *Dhfr* gene and the mutant allele obtained by deleting exon 5 with CRISPR-Cas9 engineering. (D) Representative western blot analysis of wild-type and $Dhfr^{+/\Delta}$ E12.5 head extracts (n=4). Primary antibodies are indicated on the right. Tubulin was used as a loading control. Numbers indicate relative levels. (E) DHFR activity in wild-type and $Dhfr^{+/\Delta}$ E12.5 neocortex was measured with a DHFR assay kit (Sigma-Aldrich). Enzymatic reaction kinetics were measured by spectrophotometric absorbance. (F,G) Representative images and quantification of neocortex coronal sections of E12.5 wild-type and $Dhfr^{+/\Delta}$ embryos immunostained for PAX6 and TBR2. Scale bars: 10 µm. The location of regions of interest (ROIs) (yellow box) used for quantification is indicated in the low-magnification image on the left. (H-J) Representative images and quantification of neocortex coronal sections of E12.5 wild-type and $Dhfr^{+/\Delta}$ embryos immunostained for TBR1, CTIP2 and SATB2. Scale bars: 10 µm. (K) PCA plot showing the distribution of wild-type ($Dhfr^{+/+}$) and DHFR ($Dhfr^{+/\Delta}$) embryos based on whole-genome expression profiles. (L) PCA bi-plot showing the comparison of wild-type ($Dhfr^{+/+}$) and DHFR ($Dhfr^{+/\Delta}$) embryos based on a subset of 258 genes specific to the E12.5 neocortex (data collected from Di Bella et al., 2021). Data are mean±s.d. and statistical analysis was carried out using a Mann–Whitney test.

Development (2023) 150, dev201696. doi:10.1242/dev.201696

composition. These results indicate that loss of DHFR activity promotes the generation of TBR2$^+$ progenitors at mid-corticogenesis and favors the production of SATB2$^+$ neurons by indirect neurogenesis at the expense of direct production of CTIP2$^+$ neurons.

DHFR deficiency modulates histone methylation

DHFR is a key enzyme in the one-carbon/folate metabolic pathway that has two distinct outputs: purine synthesis, which is required for DNA synthesis and cell proliferation; and synthesis of methyl groups, which is required for methylation reactions (Fig. 4A). Because it has been shown that perturbation of the methionine cycle leads to a decrease in H3K4 trimethylation, which in turn impacts gene expression (Fawal et al., 2018; Mentch et al., 2015; Shiraki et al., 2014; Shyh-Chang et al., 2013), we hypothesized that DHFR deficiency affects neurogenesis by modulating the production of methyl groups and methylation reactions. To test this, we performed biochemical assays to measure levels of THF and of the universal methyl donor SAM, and observed that both metabolites were significantly reduced in E12.5 *Dhfr*$^{+/\Delta}$ head extracts compared with wild-type samples (Fig. 4B,C). In fact, SAM levels were affected the most, halving in *Dhfr*$^{+/\Delta}$ samples (Fig. 4C). It has been shown previously that depletion in SAM levels leads to a decrease in H3K4me3 *in vitro* and this correlated with altered gene expression (Mentch et al., 2015). To test whether altered SAM levels correlated with decreased H3K4me3 in the neocortex *in vivo*, we performed western blot analysis which revealed a global loss of H3K4me3 in *Dhfr*$^{+/\Delta}$ samples compared with wild type (Fig. 4D). To go a step further, we decided to investigate whether DHFR deficiency led to changes in H3K4me3 at specific genes. To do this, we performed H3K4me3 ChIP-sequencing on neural progenitors subjected to pharmacological inhibition of DHFR *in vitro* using methotrexate (MTX), a powerful DHFR inhibitor. Our rationale for using this *in vitro* system was to ensure the observed changes in the level of H3K4me3 would be a direct consequence of inhibiting DHFR activity in neural progenitors. After DMSO or MTX treatment and ChIP-sequencing, we observed no global decrease in the level of H3K4me3 bound to neural progenitor-specific genes (Liu et al., 2017) (Fig. S4A), possibly reflecting a different sensitivity between ChIP-seq analysis and western-blot and/or a limitation due to the normalization of quantitative information using conventional ChIP-seq analysis (van Galen et al., 2016). Next, we assessed the distribution of H3K4me3 marks at sets of genes that are specific for progenitors (Kawaguchi et al., 2008) and neurons (Molyneaux et al., 2007) (Table S1). We observed a decrease in H3K4me3 binding at the TSS of VZ marker genes, while the level of H3K4me3 binding was not changed at SVZ marker genes (Fig. 4E). Concerning neuronal specification genes, some had increased H3K4me3 binding close to their TSS whereas others showed decreased H3K4me3 binding (Fig. 4E). A more detailed analysis of these neocortical layer-specific genes (Molyneaux et al., 2007) indicated a reduction in H3K4me3 on a subset of deep layer-specific genes, while the majority of upper layer-specific genes exhibited a slight increase in H3K4me3 marks in the MTX treated samples (Fig. 4F). As an example, qualitative profiling analysis revealed a substantial loss of H3K4me3 peaks at the *Bcl11b* (which encodes CTIP2) promoter in MTX-treated conditions (Fig. 4G). To confirm the effect of MTX treatment *in vivo*, we performed intraventricular *in utero* injection of MTX (20 µM) at E13.5 and analyzed the number of TBR1-, CTIP2- and SATB2-positive cells at E16.5. This analysis revealed no change in the number of TBR1$^+$ neurons with a significant reduction in the number of CTIP2$^+$ neurons at E16.5 (Fig. 4H,I), while a modest increase in the number of SATB2$^+$ neurons was observed in the lateral intermediate zone (IZ) of MTX-treated samples (Fig. S4B,C). Altogether, these findings suggest that DHFR deficiency alters epigenetic landscapes in mouse neural progenitors and this correlates with a switch in neuronal subtypes generated.

Inhibition of DHFR activity in human neural organoids promotes neurogenesis

Similar to the mouse, expression of human *DHFR* mRNA is highest in progenitors at early stages of fetal development (Fig. S5A) (Klingler et al., 2021) and at early stages of HNO development (Fig. S5B) (Kanton et al., 2019). To assess the role of human DHFR in developing neural tissue, we generated cerebral organoids, which we refer to as HNOs to follow recent nomenclature guidelines (Pasca et al., 2022), using the Lancaster protocol (Lancaster and Knoblich, 2014) and exposed them to MTX (2 µM). To specifically target neural progenitors, we treated 7 days *in vitro* (div7) neural aggregates with MTX for a duration of 3 days, with subsequent steps of HNO maturation carried out in absence of MTX (Fig. 5A). Measurement of DHFR activity in control HNOs showed a developmental reduction in DHFR activity, which is higher at div10 than at div20 (Fig. 5B), in line with the single-cell mRNA expression data (Fig. S5B). Acute 3-day MTX treatment transiently inhibited DHFR, as DHFR activity was undetectable in MTX-treated div10 HNOs but was partially recovered at div20 (Fig. 5B). Western blot analysis of human neuroepithelial samples treated with MTX revealed that inhibition of DHFR led to a global loss of H3K4me3 marks (Fig. 5C), as was shown in mouse samples (Fig. 4D). Macroscopic observation of HNOs over a 60-day time period revealed that MTX treatment stunted HNO overall growth, consistent with the role of MTX as an anti-proliferative agent (Fig. S5D). Yet in these smaller HNOs, the thickness of neocortical-like structures was increased at div40 and div60 (Fig. S5C,E) (see Materials and Methods for a description of neocortical-like structures). In contrast, the thickness of the VZ, which reflects the size of the progenitor pool, remained unchanged at div40 and div60 (Fig. S5F), suggesting that the increase in total thickness at these stages might be due solely to the enlargement of the CP in MTX-treated HNOs. To further characterize the consequences of DHFR inhibition on HNO development and maturation, we examined specific progenitor and neuronal populations in cortical-like structures at different stages of HNO culture. Because cortical-like structures in HNOs vary in size, all quantifications were made as a percentage. At div20, MTX treatment led to a small increase in the proportion of PAX6$^+$ apical progenitors and a decrease in the proportion of immature TBR1$^+$ neurons (Fig. 5D,F). In addition, the proportion of pH3-positive cells was increased in MTX-treated HNOs (Fig. 5E,F) reflecting the increased proportion of PAX6$^+$ progenitors. Together, these results indicate that inhibition of DHFR leads to an initial reduction and/or a delay in neuronal differentiation at early stages of HNO development. In contrast, at div40, we detected a reduction in the proportion of PAX6$^+$ apical progenitors associated with an overproduction of TBR2$^+$ intermediate progenitors and early-born CTIP2$^+$ deep layer neurons (Fig. 5G-I); this altered ratio was also present at div60, as we detected a persistent deficit in PAX6$^+$ apical progenitors associated with an increase in young TBR1$^+$ neurons and early-born CTIP2$^+$ neurons (Fig. 5J,L). Furthermore, at div60, late born SATB2$^+$ neurons could be observed in MTX-treated HNO, whereas they were still rare in control samples (Fig. 5K,L), suggesting that DHFR inhibition leads to an accelerated neurogenesis. Altogether, these findings indicate that inhibition of DHFR in human neural organoids leads to an

Development (2023) 150, dev201696. doi:10.1242/dev.201696

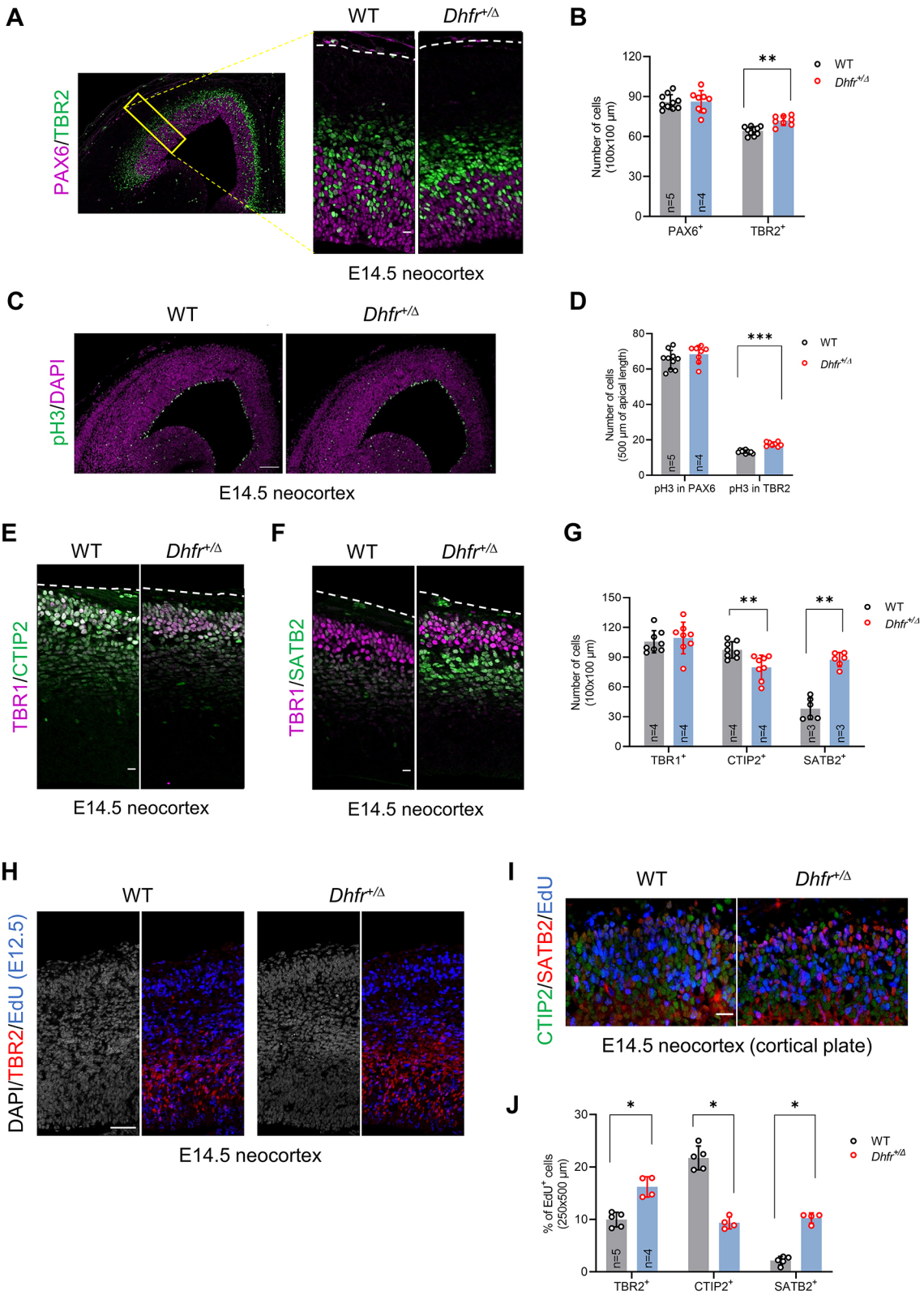

Fig. 2. Overproduction of intermediate progenitors and late-born neurons in *Dhfr*-deficient embryos. (A,B) Representative images and quantification of neocortex coronal sections of E14.5 wild-type and *Dhfr*$^{+/\Delta}$ embryos immunostained for PAX6 and TBR2. Scale bar: 10 µm. The location of regions of interest (ROIs) (yellow box) used for quantifications is indicated in the low-magnification image on the left. (C,D) Representative images and quantification of neocortex coronal sections of E14.5 wild-type and *Dhfr*$^{+/\Delta}$ embryos immunostained for pH3. Scale bar: 100 µm. (E-G) Representative images and quantification of neocortex coronal sections of E14.5 wild-type and *Dhfr*$^{+/\Delta}$ embryos immunostained for TBR1, CTIP2 and SATB2. Scale bars: 10 µm. (H-J) Representative images and quantification of neocortex coronal sections of E14.5 wild-type and *Dhfr*$^{+/\Delta}$ embryos that were injected with EdU at E12.5. Sections were immunostained for EdU, TBR2, CTIP2 and SATB2. Scale bars: 10 µm. Data are mean±s.d. and statistical analysis was carried out using a Mann–Whitney test.

Development (2023) 150, dev201696. doi:10.1242/dev.201696

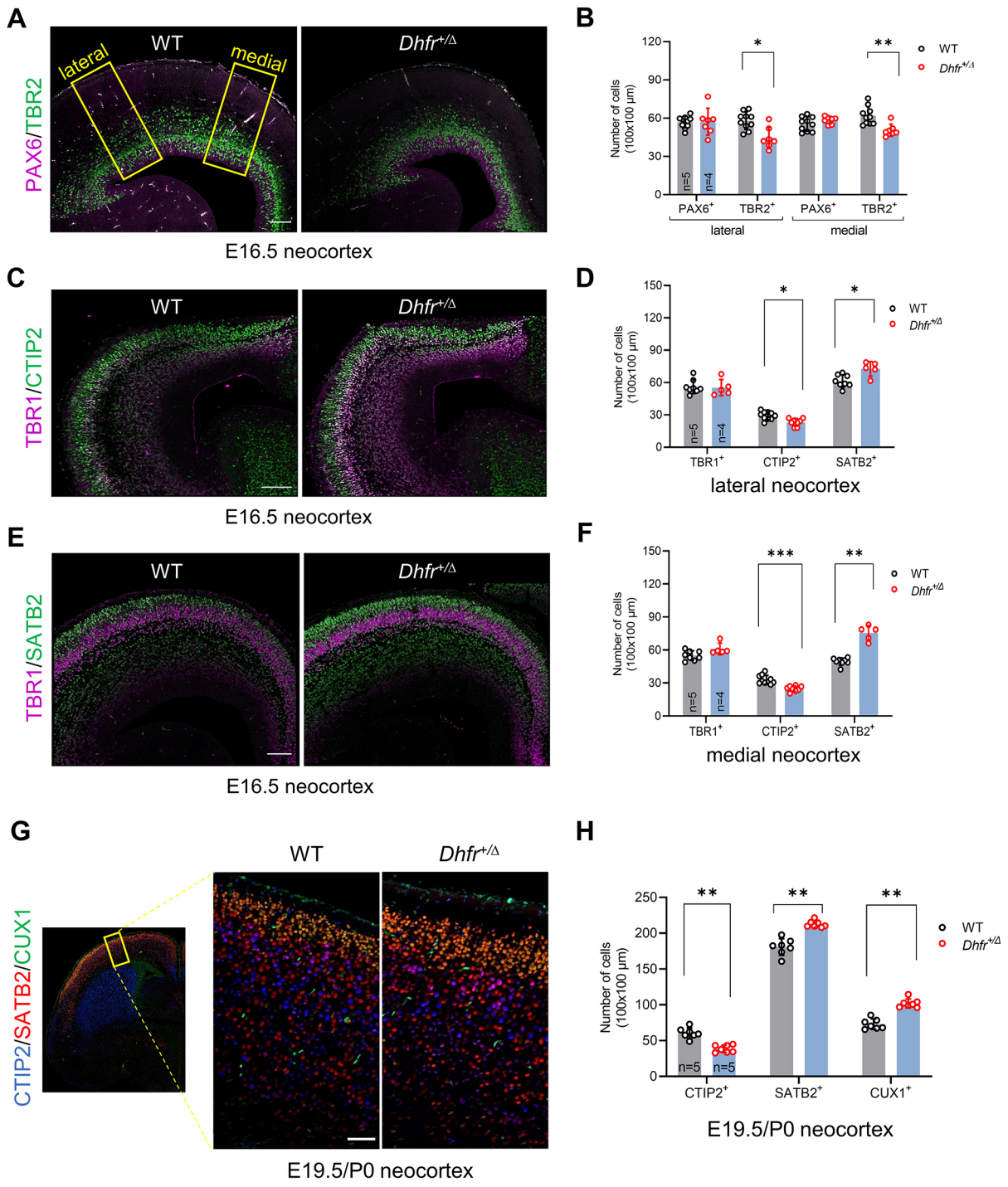

Fig. 3. Reduction in DHFR activity induces long-term changes in neocortex neuronal composition. (A-F) Representative images and quantification of neocortex coronal sections of E16.5 wild-type and *Dhfr*$^{+/\Delta}$ embryos immunostained for PAX6, TBR2, TBR1, CTIP2 and SATB2. The locations of regions of interest (ROIs) corresponding to medial and lateral neocortex used are indicated (yellow rectangles). Scale bars: 100 µm. (G,H) Representative images and quantification of neocortex coronal sections of E19.5/P0 wild-type and *Dhfr*$^{+/\Delta}$ embryos immunostained for CTIP2, SATB2 and CUX1. Scale bar: 10 µm. The ROI (yellow rectangle) used for quantifications is indicated in the low-magnification image on the left.

early developmental delay followed by increased and accelerated neuronal production.

DISCUSSION

Here, we provide evidence that DHFR, which is expressed in progenitors within a restricted time window in both mouse and human developing neocortex, plays a role in neurogenesis. Our data indicate that in both species, inhibition of DHFR activity modifies the production of neuronal subtypes by accelerating the neurogenic temporal sequence. These developmental alterations could be at the origin of altered neurodevelopment and severe neurological disorders that have been associated with mutation in DHFR or other enzymes of one-carbon/folate metabolism in humans (Cario et al., 2011; Serrano et al., 2012).

Development (2023) 150, dev201696. doi:10.1242/dev.201696

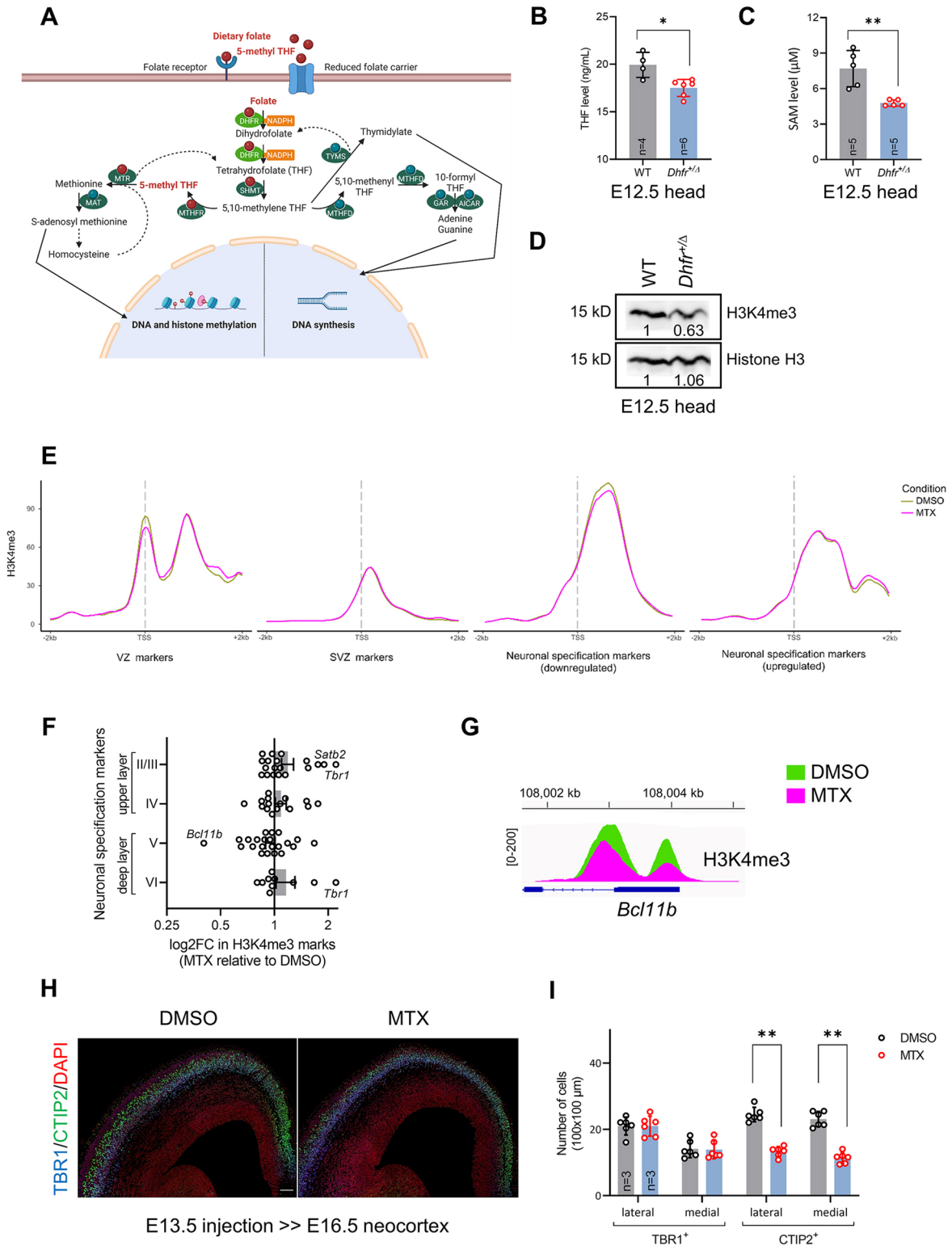

Fig. 4. DHFR inhibition modifies H3K4 trimethylation in neural progenitors. (A) Schematic representation of the 1C metabolic pathway and its outputs. Created with BioRender.com. (B,C) Levels of THF and SAM metabolites in wild-type and *Dhfr*$^{+/\Delta}$ E12.5 head extracts. THF levels were measured with a competitive inhibition enzyme immunoassay kit (Cloud-Clone) by quantifying pre-coated antibody binding with colorimetric absorbance. SAM levels were measured with Bridge-It assay kit (Mediomics) by determining DNA-MetJ protein complex formation in the presence of SAM as ligand. (D) Representative western blot analysis of wild-type and *Dhfr*$^{+/\Delta}$ E12.5 head extracts (n=4). Primary antibodies are indicated on the right. Histone H3 was used as a loading control. Numbers indicate relative levels. (E) Metagene analyses of H3K4me3 at selected marker genes after 72 h of MTX (2 µM) treatment in mouse neurosphere cultures (n=2). (F) Graphical representation of specific changes in methylation levels at neuronal specification genes. Each dot represents a gene and the mean peak intensity±s.e.m. for each layer. (G) Visualization of H3K4me3 peaks at *Bcl11b* promoter using ChIP-seq read mapping data. (H,I) Representative images and quantification of neocortex coronal sections of E16.5 DMSO and MTX (20 µM)-injected wild-type embryos immunostained for TBR1, CTIP2 and DAPI. Scale bar: 100 µm. Data are mean±s.d. and statistical analysis was carried out using a Mann–Whitney test.

Development (2023) 150, dev201696. doi:10.1242/dev.201696

We report the generation of *Dhfr*$^{+/\Delta}$ haploinsufficient embryos that exhibit alterations in neurogenesis and neuronal subtype production. In the *Dhfr*$^{+/\Delta}$ mutant mouse line, DHFR protein levels and DHFR activity are halved in the embryonic neocortex, revealing an absence of compensatory mechanisms from the wild-type allele. Absence of compensatory mechanisms also applies to humans, as a two-fold reduction in DHFR protein levels and activity was reported in individuals carrying a heterozygous point mutation in *DHFR* (Banka et al., 2011; Cario et al., 2011). Although it is generally admitted that metabolic pathways are not sensitive to gene dose due to buffering by other components of the network, this is not true for some rate-limiting enzymes (Johnson et al., 2019). Despite the important role of DHFR in DNA replication, we observed no decreased proliferation and no increased cell death in the neocortex of *Dhfr*$^{+/\Delta}$ heterozygous embryos, indicating that one copy of wild-type *Dhfr* is sufficient to sustain purine synthesis. Conversely, we observed decreased levels of SAM and H3K4 trimethylation in *Dhfr*$^{+/\Delta}$ embryonic neocortex, indicating that DHFR activity is rate-limiting for the methionine cycle and methyl group synthesis in the neural tissue. In a previously described *Dhfr* mutant mouse line (*Ora*) generated by ENU mutagenesis, it was reported that heterozygous animals, which exhibited reduced DHFR activity, survived to adulthood with tissue-specific alterations in folate abundance and distribution, and perturbed stress erythropoiesis (Thoms et al., 2016). These data, together with our data, raise the possibility that *Dhfr* is a haploinsufficient gene and suggests that human carriers of heterozygous mutations may have subtle alterations of the blood and brain compartments.

Recent single-cell RNA-sequencing data showed that *Dhfr* mRNA is expressed at high levels in neural progenitors at early stages of development and is downregulated in apical progenitors at later stages, as well as in intermediate progenitors and differentiating neurons (Di Bella et al., 2021; Kanton et al., 2019; Telley et al., 2019). This dynamic expression pattern suggests that DHFR may play a specific function in apical progenitors. Analyses of neocortex development in *Dhfr*$^{+/\Delta}$ haploinsufficient mouse embryos revealed an initial developmental delay followed by an acceleration of indirect neurogenesis, culminating in the overproduction of late-born neurons at the expense of early-born neurons. Accelerated indirect neurogenesis was also observed in HNOs treated with MTX at an early stage of development, strongly suggesting that these phenotypes are a direct consequence of DHFR inhibition in neural progenitors and not due to systemic causes. However, based on our data, we cannot completely exclude the possibility that, in mice, DHFR inhibition impacts other neural cell types that are known to influence apical progenitor behavior (Villalba et al., 2021), which then could non-autonomously contribute to the observed phenotypes. These phenotypes are reminiscent of microcephalic features observed in individuals harboring mutations *DHFR* (Banka et al., 2011), which could be due to premature differentiation leading to depletion of neural progenitor pools. Recent work studying the impact of folate-deficient diet on fetal corticogenesis in the mouse reported alterations in the production of neuronal subtypes that are similar to those observed in *Dhfr*$^{+/\Delta}$ haploinsufficient embryos (Harlan De Crescenzo et al., 2021). However, the impact of folate-deficient diet on progenitors was different and was associated with increased cell death in the neocortex (Harlan De Crescenzo et al., 2021), suggesting that a folate-deficient diet could have broad deleterious consequences on the pregnant dam that indirectly impact fetal corticogenesis.

It is well established that developmental transitions occurring during neocortex development involve chromatin and epigenetic modifications in neural progenitors (Albert et al., 2017; Hirabayashi and Gotoh, 2010; Koo et al., 2022). Here, we show that inhibition of DHFR in mouse neural progenitors *in vitro* leads to discrete changes in H3K4me3 marks on neuronal specification genes. Indeed, after MTX treatment, a number of genes expressed in early-born neurons have less H3K4me3 bound close to the TSS, whereas some genes expressed in late-born neurons have more H3K4me3 marks but these are localized further away from the TSS. Although these changes in epigenetic marks are consistent with the observed changes in neuronal subtypes in *Dhfr*$^{+/\Delta}$ embryos *in vivo*, further experiments would be needed to establish causality and to identify primary versus secondary changes in H3K4me3 levels. Nevertheless, these results suggest that variations in DHFR activity could influence the epigenetic landscape in apical progenitors and that these epigenetic modifications may set the stage for production of the different neuronal subtypes. Indeed, recent single-cell analyses of chromatin and gene-regulatory dynamics in the developing brain suggested that progenitors entering the cell cycle may be epigenetically primed toward future cell states (Trevino et al., 2021). The fact that histone modifications are stable epigenetic marks may underlie the long-term effects of inhibiting DHFR activity at early stages of neocortex development, as we have shown previously on neural progenitors *in vitro* (Fawal et al., 2018).

Our study identified a conserved function for DHFR in controlling neurogenesis. Indeed, at mid-corticogenesis, reducing DHFR activity led to increased production of SATB2$^+$ neurons in both mouse and human contexts. In the mouse, we observed a switch from CTIP2$^+$ to SATB2$^+$ neurons, whereas in the human context, we observed an increase of both types of neurons. This difference could be due to the fact that TBR2$^+$ intermediate progenitors, which are increased following DHFR inhibition both in mouse and human contexts, have different neuronal outputs in both species. Indeed, a recent lineage-tracing study in the mouse estimated that TBR2$^+$ progenitors generate ∼90% of SATB2$^+$ neurons but only ∼50% of CTIP2$^+$ neurons present in the neocortex (Huilgol et al., 2023). In humans, however, intermediate progenitors are hypothesized to give rise to the majority of projection neurons regardless of their subtype (Lui et al., 2011). In fact, in human developing embryos, TBR2$^+$ progenitors are present from the earliest stages of neurogenesis, and single-cell transcriptomics identified various subpopulations of TBR2$^+$ progenitors (Fan et al., 2020; Pebworth et al., 2021), including one subtype that may give rise to deep layer neurons (Fan et al., 2020). Although it is well known that apical progenitors generate neurons both directly and indirectly, the molecular mechanisms governing the switch from one to the other neurogenic process are not well characterized. In the mouse it was estimated that 5% of apical progenitors produce neurons (mostly CTIP2$^+$) directly at E12.5 and that the switch between direct and indirect neurogenesis involves Robo and Dll1 signaling (Cárdenas et al., 2018), as well as modifications of cell cycle parameters (Roussat et al., 2023). In the future, it would be interesting to assess the link between DHFR and these different pathways. One defining feature of indirect neurogenesis is that it is a hallmark of mammalian neocortex evolution. Indeed, direct neurogenesis with limited neuronal production dominates avian and reptilian paleocortex, whereas indirect neurogenesis predominates in mouse neocortex (Cárdenas et al., 2018). In the human neocortex, indirect neurogenesis is vastly expanded and accounts for the large increase in neuron numbers (Hansen et al., 2010; Lewitus et al., 2014; Namba and Huttner, 2017). Whether this evolutionary innovation was driven, at least in part, by evolutionary changes in 1C metabolism is an interesting question for future research (Namba et al., 2021).

Development (2023) 150, dev201696. doi:10.1242/dev.201696

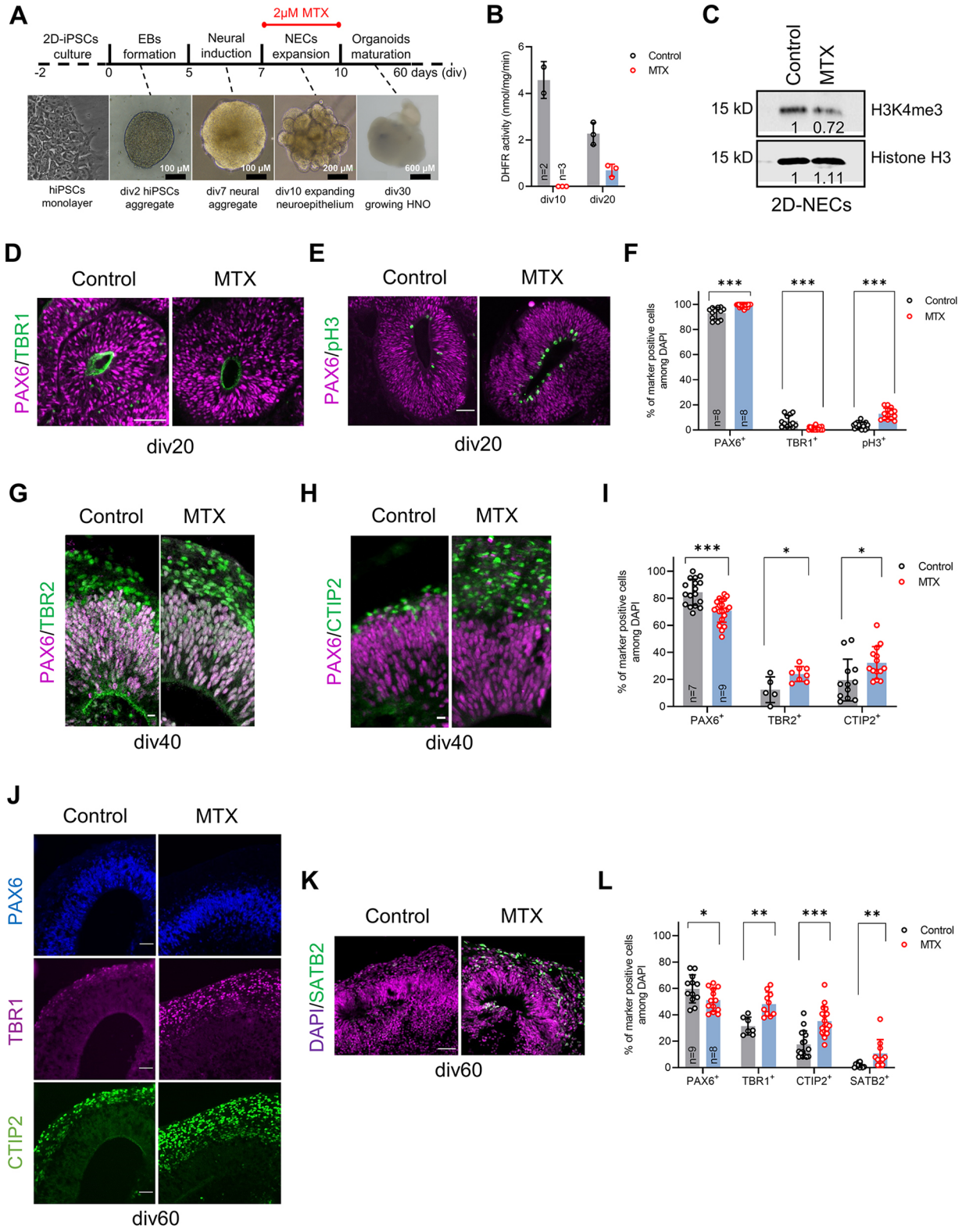

Fig. 5. DHFR deficiency accelerates the neurogenic program in HNOs. (A) Timeline of the protocol used to generate HNOs. The time window of MTX treatment is indicated in red. (B) DHFR activity in pooled DMSO- (control) or MTX-treated (*n*=2 or 3 replicates of six to eight pooled HNOs) HNOs at two different time points. DHFR activity was measured with a DHFR assay kit (Sigma-Aldrich). Enzymatic reaction kinetics were measured by spectrophotometric absorbance. (C) Representative western blot analysis of human neuroepithelial cells (2D-NECs) treated with DMSO (control) or with MTX (*n*=4). Primary antibodies are indicated on the right. Histone H3 was used as a loading control. Numbers indicate relative levels. (D-F) Representative images and quantification of control and MTX-treated HNOs immunostained for pH3, PAX6 and TBR1 at div20. Scale bars: 50 µm. (G-I) Representative images and quantification of control and MTX-treated HNO immunostained for PAX6, TBR2 and CTIP2 at div40. Scale bars: 10 µm. (J-L) Representative images and quantification of control and MTX-treated HNOs immunostained for PAX6, TBR1, CTIP2 and SATB2 at div60. Scale bars: 50 µm. Data are mean±s.d. (*n*=7-12 organoids with 15-20 cortical-like structures analyzed using a Mann–Whitney test).

Development (2023) 150, dev201696. doi:10.1242/dev.201696

MATERIALS AND METHODS

Animals

Dhfr$^{+/\Delta}$ mice were generated by CRISPR/Cas9-mediated excision of exon 5 (see supplementary Materials and Methods for further details). Mice were kept in a 129S4/C57Bl6J mixed background. The gender of embryos was not tested, littermates of each genotype were randomly assigned to experimental groups. All experimental procedures were pre-approved and carried out in compliance with the guidelines provided by the national Animal Care and Ethics Committee (APAFIS#1289-2015110609133558 v5) following Directive 2010/63/EU.

Genotyping

Genomic DNA was isolated from mouse tail and genotyping was performed using 2x PCR Taq MasterMix (abm). The PCR amplification was performed using Veriti thermal cycler (ThermoFisher) followed by agarose gel electrophoresis.

Pluripotent stem cells

Human iPSCs were obtained from Leiden University Medical Center hiPSC core facility (LUMC0004iCTRL). Cells were amplified with mTesR+ medium (STEMCELL Technologies) on h-ES qualified Matrigel (Corning) coating and stored frozen in liquid nitrogen. HNO were generated using STEMdiff cerebral organoid kit (STEMCELL Technologies) by following manufacturer instructions. Cells are tested for mycoplasma every 6 months using the mycoAlert kit (Lonza).

2D-neuroepithelial cell culture

2D-neuroepithelial cells (2D-NECs) were derived from human-iPSCs using the STEMdiff SMADi neural induction kit (STEMCELL Technologies) by following the manufacturer's instructions for the monolayer culture. They were then grown and amplified for two additional passages, using Accutase (STEMCELL Technologies) in STEMdiff neural progenitor medium (STEMCELL Technologies) on Matrigel and stored in liquid nitrogen using STEMdiff neural progenitor freezing medium (STEMCELL Technologies). For inhibition of DHFR activity in 2D-neuroepithelial cells, 50% confluent cells were treated for 3 days with 2 µM MTX diluted in growing medium.

Generation and maintenance of HNO

For every single batch of HNOs, one vial of iPSCs was defrosted every 3-4 days and cells were allowed to reach 70-80% confluence in mTesR+ medium. HNOs were generated using STEMdiff cerebral organoid kit (STEMCELL Technologies), following the manufacturer's instructions, until div60 as the final time point. For acute inhibition of DHFR activity in HNO, neuroepithelial aggregates were treated at div7 with 2 µM MTX (Sigma-Aldrich) freshly diluted in expansion medium, for 3 days.

Histochemistry

Mouse embryonic brains were embedded in paraffin wax, agarose or OCT; HNOs were embedded in OCT for microtome, vibratome or cryostat sectioning. Sections were permeabilized and incubated with antibodies diluted in blocking solution (1-3% BSA, 1-3% FBS, 0.5-1% Tween 20 and PBS) overnight at 4°C (see Table S3 for antibody details). For birthdating experiments, EdU (dissolved in PBS at 5 mg/ml, 25 µg/g body weight) was injected intraperitoneally at E12.5 and samples were collected at E14.5. Histological detection of EdU was performed using the Click-iT EdU cell proliferation kit (ThermoFisher) according to the manufacturer's instructions. For further details see supplementary Materials and Methods.

Imaging

Fluorescent images of tissue and organoid sections were captured with SP8 inverted scanning confocal microscope (Leica Biosystems) or Eclipse 80i fluorescence microscope (Nikon).

Western blot

For protein extraction, mouse and human tissues were obtained by incubating in lysis buffer [150 mM NaCl, 50 mM Tris-HCl (pH 7.4), 0.5 mM EDTA, 2 mM Na_3VO_4, 1% NP-40, 0.5 mM EGTA and 0.1 mM PMSF] supplemented with protease inhibitors for 1 h on ice. Protein lysates were vortexed, ultrasonicated for five cycles (Bioblock), and centrifuged at 16,100 ***g*** for 10 min. Protein concentration in the supernatant was determined using a DC protein assay (Bio-Rad). Lysates were then denatured by boiling in 4× loading buffer [100 mM Tris-HCl (pH 6.8), 8% SDS, 40% glycerol, 4% β-mercaptoethanol and bromophenol blue) before loading and electrophoresis on 4-20% or 12% SDS-PAGE gel using mini-PROTEAN electrophoresis chamber (Bio-Rad). Proteins were transferred onto a 0.45 µm PVDF (Millipore) or nitrocellulose membrane (GE Healthcare), which was blocked for 30 min and incubated with primary antibody in 5% nonfat dry milk in TBST [20 mM Tris, 150 mM NaCl, and 0.05% Tween 20 (pH 7.6)] overnight at 4°C. The membrane was then incubated with HRP-conjugated secondary antibodies in 5% nonfat dry milk in TBST. Immunoreactive bands were generated by adding Lumi-Light plus chemiluminescent substrates (Roche). See Table S3 for antibody details.

RNA-sequencing

Brains from E12.5 wild-type and *Dhfr*$^{+/\Delta}$ embryos were collected and the neocortex was dissected. The tissue was mechanically dissociated to form a cell pellet. RNA was isolated from the cell pellet using Trizol reagent (Invitrogen) according to the manufacturer's instructions and eluted into 35 µl nuclease-free water. Eluted RNAs were then stored at −80°C. RNA quality and integrity (RIN>7) were verified by electrophoresis using a 2100 Bioanalyzer system (Agilent). The whole procedure going from the dissociation to RNA preparation was performed on six animals (n=3 wild type and n=3 *Dhfr*$^{+/\Delta}$) obtained from two different littermates.

RNA libraries were prepared using NEBNext ultra II reagent (New England Biolabs) and RNA sequencing on neocortical samples were performed by IntegraGen (https://integragen.com) using an Illumina NovaSeq 6000 S2 sequencing system (paired-end sequencing, 100 bp reads, 35 M reads/sample).

Differential analysis was applied per genotype (wild type vs *Dhfr*$^{+/\Delta}$) by taking into consideration of litter effects using DESeq2 v1.32.0 (Love et al., 2014), available as an R package in Bioconductor (www.bioconductor.org). The raw read counts were normalized using RLE methods generating and the log2 Fold Change (log2FC) values were computed. We used principal component analysis (PCA) to cluster samples based on their expression levels. Data representation of the scaled PCA was generated using the ggplot2 package (https://ggplot2.tidyverse.org).

ChIP-sequencing

Neural progenitor cells cultured as free-floating neurospheres were treated with DMSO or 2 µM MTX for 72 h. The cells were further processed for DNA extraction according to the previously described method (Fawal et al., 2018).

GenomEast (http://genomeast.igbmc.fr) performed DNA quantification with Qubit (Invitrogen) and processed 1.5-10 ng of double-stranded purified DNA to generate libraries using MicroPlex library preparation kit v2 (Diagenode). Amplified libraries were purified with Agencourt AMPure XP beads (Beckman Coulter) and sequenced on an Illumina Hiseq 4000 sequencer (single-end sequencing, read length 50, minimum 45 M reads/sample). Sequence reads were mapped to the *Mus musculus* genome assembly (mm10) using Bowtie (Langmead et al., 2009). Peak calling was carried out using MACS v2.1.1 (Zhang et al., 2008; Feng et al., 2012). Peaks were annotated to the Ensembl release 94 using HOMER software (http://homer.ucsd.edu/homer/ngs/annotation.html). Peaks from different conditions and replicates were merged to form a consensus peak set. The read coverage for each sample was calculated with multicov function from bedtools v2.26.0 (Quinlan and Hall, 2010). Differential analysis was applied per condition (DMSO versus MTX) using DESeq2 v1.20.0 (Love et al., 2014) to calculate log2 fold change of H3K4me3 ChIP-sequencing read counts in MTX condition versus DMSO condition. Data representation of the differential binding analysis corresponds to a strong change in peak heights at the promoter or gene body. For further details see supplementary Materials and Methods.

RT-PCR and qRT-PCR

RNA was extracted from E12.5 head (for RT-PCR) or E12.5 neocortex (for qRT-PCR) using Trizol reagent according to the manufacturer's instructions. 1 µg RNA was used for reverse transcription.

Development (2023) 150, dev201696. doi:10.1242/dev.201696

For RT-PCR, 1 µl diluted cDNA (10-fold) was mixed with 2x PCR Taq MasterMix containing 1 µM of each primer, and PCR amplification was performed followed by agarose gel electrophoresis.

For quantitative PCR, cDNAs were diluted (10-, 100- and 1000-fold) and processed in triplicate for each dilution. 10 µl diluted cDNA was mixed with 10 µl premix Evagreen (Bio-Rad) containing 1 µM of each primer, and the PCR program was run for 40 cycles on CFX96 Real-Time PCR system (Bio-Rad). For further details see supplementary Materials and Methods.

Metabolic assays

DHFR activity was detected with DHFR assay kit (Sigma-Aldrich). Mouse and human tissues were suspended in 200 µl of Cellytic MT reagent (Sigma-Aldrich) supplemented with protease inhibitors and lysed mechanically using glass beads (Sigma-Aldrich). Lysates were precleared by centrifugation at 16,100 ***g*** for 10 min. The supernatant was mixed in quartz cuvette (Hellma) with 6 µl of NADPH, 5 µl of DHFA and 800 µl of assay buffer provided in the kit, and reaction kinetics were monitored by spectrophotometric absorbance at 340 nm for 2-3 min. The readouts were normalized to the protein concentration in the supernatant at 280 nm.

THF levels were analyzed based on a competitive inhibition enzyme immunoassay kit (Cloud-Clone). Dissected E12.5 head samples were suspended in 120 µl of Cellytic MT reagent supplemented with protease inhibitors followed by mechanical dissociation with a pipette tip for cell lysis and incubated on ice for 30 min. Lysates were precleared by ultrasonication and cell debris were pelleted by centrifugation at 16,100 ***g*** for 10 min. The supernatant was separated and kept with kit components at room temperature for 10 min. 50 µl of serially diluted standard or samples were added in pre-coated wells provided in the kit followed by incubation and wash steps according to the manufacturer's instructions. The absorbance was measured at 450 nm using Varioskan flash (ThermoFisher) and readouts from standard were plotted to construct a standard curve for estimating THF concentration.

SAM levels were determined by Bridge-It assay kit (Mediomics) based on biosensor fluorescence. Dissected E12.5 head samples were suspended in 100 µl of supplied CM buffer solution supplemented with protease inhibitors followed by mechanical dissociation with a pipette tip for cell lysis and incubated at room temperature for 30 min. Cell debris were pelleted by centrifugation at 16,100 ***g*** for 10 min and supernatant was separated. In a black 96-well microplate (ThermoFisher), 10 µl of standard mix (1 mM SAM) was serially diluted with Buffer S provided in the kit. 10 µl of standard mix and 50 µl of samples were then incubated with supplied assay solution at a total volume of 100 µl at room temperature for 30 min in dark. The signal intensity of fluorescence excited at 485 nm for 1 s was measured at 665 nm using Varioskan flash. The readouts from standard were plotted to construct a standard curve for estimating SAM concentration.

Quantifications and statistical analyses

Fluorescent images were captured with SP8 inverted scanning confocal microscope (Leica Biosystems) or Eclipse 80i fluorescence microscope (Nikon). The microscopic and macroscopic images were acquired with Eclipse TS100 inverted microscope (Nikon) and SMZ18 stereomicroscope (Nikon), respectively. Images were exported as TIFF files and quantification was performed manually with ImageJ (NIH) on defined regions of interest (ROIs). For mouse embryos, one ROI was counted at E12.5 and E14.5, and two ROIs were counted at E16.5 (positioning of ROI at each stage is shown in main figures). Embryos were collected from different litters and 100-500 cells were counted per hemisphere using multiple sections. Counts were normalized to an area of 100 µm of apical surface×100 µm of radial length. For organoids, quantifications were performed on cortical-like structures that were selected based on morphometric parameters (structures located at the periphery of the organoids, presence of a lumen, elongated shape of pseudostratified nuclei and a densely packed ventricular zone at least five nuclei thick). We confirmed that these morphometric parameters identified cortical-like structures by performing EMX1 immunostaining (Fig. S5C). One ROI was counted for each cortical-like structure, 100-500 cells were counted on different cortical-like structures from different HNOs and quantifications were expressed as percentage (using DAPI to count total cell number). For western blots, tissue lysates were collected from four mouse embryos for each genotype and the western blots were carried out twice with independent samples. For metabolic assays, tissue extracts were obtained from at least four to seven mouse embryos for each genotype. The exact number of samples for each experiment is provided in each graph and in Table S2. For experiments involving a pair of conditions, statistical significance between the two sets of data were analyzed with Mann–Whitney test with Holm-Šidák adjusted *P*-values using Prism9 (GraphPad). Statistically significant differences are reported at $*P<0.05$, $**P<0.01$ and $***P<0.001$.

Acknowledgements

We thank Alain Vincent and Eric Agius for critical reading of the manuscript. We acknowledge the help and contribution of the ANEXPLO mouse facility and the TRI imaging platform at the CBI. We also thank the CBI-bigA facility engineers for their help and feedback during the raw data processing, the statistical analysis and the data visualization of sequencing data. Sequencing for the ChIP-Seq analysis was performed by the GenomEast platform, which is a member of the 'France Génomique' consortium (ANR-10-INBS-0009). Both CNRS and Université de Toulouse provided core funding.

Competing interests

The authors declare no competing or financial interests.

Author contributions

Conceptualization: S.S., T.J., M.F., A.D.; Methodology: S.S., T.J., C.A., T.Y., M.F.; Software: D.O., T.Y.; Validation: S.S., T.J., M.F., A.D.; Formal analysis: S.S., T.J., D.O., C.A., T.Y., M.F., A.D.; Investigation: S.S., T.Y., M.F.; Resources: T.J., A.D.; Data curation: S.S., T.J., D.O., C.A., T.Y., M.F., A.D.; Writing - original draft: S.S., A.D.; Writing - review & editing: T.J., D.O., C.A., M.F., A.D.; Visualization: D.O., C.A., M.F.; Supervision: T.J., A.D.; Project administration: T.J., M.F., A.D.; Funding acquisition: A.D.

Funding

This work was funded by the Fondation pour la Recherche Médicale (DEQ20180339174) and the Agence Nationale de la Recherche (ANR-21-CE16-0024-01). S.S. is the recipient of a 3-year PhD scholarship from the Ministère de l'Enseignement Supérieur et de la Recherche Scientifique. Open Access funding provided by the Agence Nationale de la Recherche. Deposited in PMC for immediate release.

Data availability

RNA-Seq and ChIP-Seq data have been deposited in GEO under accession numbers GSE206406 and GSE206407.

Peer review history

The peer review history is available online at https://journals.biologists.com/dev/lookup/doi/10.1242/dev.201696.reviewer-comments.pdf.

References

Albert, M., Kalebic, N., Florio, M., Lakshmanaperumal, N., Haffner, C., Brandl, H., Henry, I. and Huttner, W. B. (2017). Epigenome profiling and editing of neocortical progenitor cells during development. *EMBO J.* **36**, 2642-2658. doi:10.15252/embj.201796764

Banka, S., Blom, H. J., Walter, J., Aziz, M., Urquhart, J., Clouthier, C. M., Rice, G. I., de Brouwer, A. P. M., Hilton, E., Vassallo, G. et al. (2011). Identification and characterization of an inborn error of metabolism caused by dihydrofolate reductase deficiency. *Am. J. Hum. Genet.* **88**, 216-225. doi:10.1016/j.ajhg.2011.01.004

Cárdenas, A., Villalba, A., De Juan Romero, C., Picó, E., Kyrousi, C., Tzika, A. C., Tessier-Lavigne, M., Ma, L., Drukker, M., Cappello, S. et al. (2018). Evolution of cortical neurogenesis in amniotes controlled by robo signaling levels. *Cell* **174**, 590-606.e21. doi:10.1016/j.cell.2018.06.007

Cario, H., Smith, D. E. C., Blom, H., Blau, N., Bode, H., Holzmann, K., Pannicke, U., Hopfner, K.-P., Rump, E.-M., Ayric, Z. et al. (2011). Dihydrofolate reductase deficiency due to a homozygous DHFR mutation causes megaloblastic anemia and cerebral folate deficiency leading to severe neurologic disease. *Am. J. Hum. Genet.* **88**, 226-231. doi:10.1016/j.ajhg.2011.01.007

Clare, C. E., Brassington, A. H., Kwong, W. Y. and Sinclair, K. D. (2018). One-carbon metabolism: linking nutritional biochemistry to epigenetic programming of long-term development. *Annu. Rev. Anim. Biosci.* **7**, 263-287. doi:10.1146/annurev-animal-020518-115206

Di Bella, D. J., Habibi, E., Stickels, R. R., Scalia, G., Brown, J., Yadollahpour, P., Yang, S. M., Abbate, C., Biancalani, T., Macosko, E. Z. et al. (2021). Molecular logic of cellular diversification in the mouse cerebral cortex. *Nature* **595**, 554-559. doi:10.1038/s41586-021-03670-5

Ducker, G. S. and Rabinowitz, J. D. (2017). One-carbon metabolism in health and disease. *Cell Metab.* **25**, 27-42. doi:10.1016/j.cmet.2016.08.009

Eze, U. C., Bhaduri, A., Haeussler, M., Nowakowski, T. J. and Kriegstein, A. R. (2021). Single-cell atlas of early human brain development highlights heterogeneity of human neuroepithelial cells and early radial glia. *Nat. Neurosci.* **24**, 584-594. doi:10.1038/s41593-020-00794-1

Fan, X., Fu, Y., Zhou, X., Sun, L., Yang, M., Wang, M., Chen, R., Wu, Q., Yong, J., Dong, J. et al. (2020). Single-cell transcriptome analysis reveals cell lineage specification in temporal-spatial patterns in human cortical development. *Sci. Adv.* **6**, eaaz2978. doi:10.1126/sciadv.aaz2978

Fawal, M.-A., Jungas, T., Kischel, A., Audouard, C., Iacovoni, J. S. and Davy, A. (2018). Cross talk between one-carbon metabolism, Eph signaling, and histone methylation promotes neural stem cell differentiation. *Cell Rep.* **23**, 2864-2873.e7. doi:10.1016/j.celrep.2018.05.005

Fawal, M.-A., Jungas, T. and Davy, A. (2021). Inhibition of DHFR targets the self-renewing potential of brain tumor initiating cells. *Cancer Lett.* **503**, 129-137. doi:10.1016/j.canlet.2021.01.026

Feder, J. N., Assaraf, Y. G., Seamer, L. C. and Schimke, R. T. (1989). The pattern of dihydrofolate reductase expression through the cell cycle in rodent and human cultured cells. *J. Biol. Chem.* **264**, 20583-20590. doi:10.1016/S0021-9258(19)47102-0

Feng, J., Liu, T., Qin, B., Zhang, Y. and Liu, X. S. (2012). Identifying ChIP-seq enrichment using MACS. *Nat. Protoc.* **7**, 1728-1740. doi:10.1038/nprot.2012.101

Götz, M., Stoykova, A. and Gruss, P. (1998). Pax6 controls radial glia differentiation in the cerebral cortex. *Neuron* **21**, 1031-1044. doi:10.1016/S0896-6273(00)80621-2

Hansen, D. V., Lui, J. H., Parker, P. R. L. and Kriegstein, A. R. (2010). Neurogenic radial glia in the outer subventricular zone of human neocortex. *Nature* **464**, 554-561. doi:10.1038/nature08845

Harlan De Crescenzo, A., Panoutsopoulos, A. A., Tat, L., Schaaf, Z., Racherla, S., Henderson, L., Leung, K.-Y., Greene, N. D. E., Green, R. and Zarbalis, K. S. (2021). Deficient or excess folic acid supply during pregnancy alter cortical neurodevelopment in mouse offspring. *Cereb. Cortex* **31**, 635-649. doi:10.1093/cercor/bhaa248

Haubensak, W., Attardo, A., Denk, W. and Huttner, W. B. (2004). Neurons arise in the basal neuroepithelium of the early mammalian telencephalon: a major site of neurogenesis. *Proc. Natl. Acad. Sci. USA* **101**, 3196-3201. doi:10.1073/pnas.0308600100

Hirabayashi, Y. and Gotoh, Y. (2010). Epigenetic control of neural precursor cell fate during development. *Nat. Rev. Neurosci.* **11**, 377-388. doi:10.1038/nrn2810

Huilgol, D., Levine, J. M., Galbavy, W., Wang, B.-S., He, M., Suryanarayana, S. M. and Huang, Z. J. (2023). Direct and indirect neurogenesis generate a mosaic of distinct glutamatergic projection neuron types in cerebral cortex. *Neuron*. doi:10.1016/j.neuron.2023.05.021

Johnson, A. F., Nguyen, H. T. and Veitia, R. A. (2019). Causes and effects of haploinsufficiency. *Biol. Rev. Camb. Philos. Soc.* **94**, 1774-1785. doi:10.1111/brv.12527

Kanton, S., Boyle, M. J., He, Z., Santel, M., Weigert, A., Sanchís-Calleja, F., Guijarro, P., Sidow, L., Fleck, J. S., Han, D. et al. (2019). Organoid single-cell genomic atlas uncovers human-specific features of brain development. *Nature* **574**, 418-422. doi:10.1038/s41586-019-1654-9

Kawaguchi, A., Ikawa, T., Kasukawa, T., Ueda, H. R., Kurimoto, K., Saitou, M. and Matsuzaki, F. (2008). Single-cell gene profiling defines differential progenitor subclasses in mammalian neurogenesis. *Development* **135**, 3113-3124. doi:10.1242/dev.022616

Klingler, E., Francis, F., Jabaudon, D. and Cappello, S. (2021). Mapping the molecular and cellular complexity of cortical malformations. *Science* **371**, eaba4517. doi:10.1126/science.aba4517

Koo, B., Lee, K.-H., Ming, G.-L., Yoon, K.-J. and Song, H. (2022). Setting the clock of neural progenitor cells during mammalian corticogenesis. *Semin. Cell Dev. Biol.* **142**, 43-53. doi:10.1016/j.semcdb.2022.05.013

Lancaster, M. A. and Knoblich, J. A. (2014). Generation of cerebral organoids from human pluripotent stem cells. *Nat. Protoc.* **9**, 2329-2340. doi:10.1038/nprot.2014.158

Langmead, B., Trapnell, C., Pop, M. and Salzberg, S. L. (2009). Ultrafast and memory-efficient alignment of short DNA sequences to the human genome. *Genome Biol.* **10**, R25. doi:10.1186/gb-2009-10-3-r25

Lewitus, E., Kelava, I., Kalinka, A. T., Tomancak, P. and Huttner, W. B. (2014). An adaptive threshold in mammalian neocortical evolution. *PLoS Biol.* **12**, e1002000. doi:10.1371/journal.pbio.1002000

Liu, J., Wu, X., Zhang, H., Pfeifer, G. P. and Lu, Q. (2017). Dynamics of RNA Polymerase II Pausing and Bivalent Histone H3 Methylation during Neuronal Differentiation in Brain Development. *Cell Rep.* **20**, 1307-1318. doi:10.1016/j.celrep.2017.07.046

Love, M. I., Huber, W. and Anders, S. (2014). Moderated estimation of fold change and dispersion for RNA-seq data with DESeq2. *Genome Biol.* **15**, 550. doi:10.1186/s13059-014-0550-8

Lui, J. H., Hansen, D. V. and Kriegstein, A. R. (2011). Development and evolution of the human neocortex. *Cell* **146**, 18-36. doi:10.1016/j.cell.2011.06.030

Mentch, S. J., Mehrmohamadi, M., Huang, L., Liu, X., Gupta, D., Mattocks, D., Gómez Padilla, P., Ables, G., Bamman, M. M., Thalacker-Mercer, A. E. et al. (2015). Histone methylation dynamics and gene regulation occur through the sensing of one-carbon metabolism. *Cell Metab.* **22**, 861-873. doi:10.1016/j.cmet.2015.08.024

Miyata, T., Kawaguchi, A., Saito, K., Kawano, M., Muto, T. and Ogawa, M. (2004). Asymmetric production of surface-dividing and non-surface-dividing cortical progenitor cells. *Development* **131**, 3133-3145. doi:10.1242/dev.01173

Molyneaux, B. J., Arlotta, P., Menezes, J. R. L. and Macklis, J. D. (2007). Neuronal subtype specification in the cerebral cortex. *Nat. Rev. Neurosci.* **8**, 427-437. doi:10.1038/nrn2151

Namba, T. and Huttner, W. B. (2017). Neural progenitor cells and their role in the development and evolutionary expansion of the neocortex. *Wiley Interdiscip. Rev. Dev. Biol.* **6**, e256. doi:10.1002/wdev.256

Namba, T., Nardelli, J., Gressens, P. and Huttner, W. B. (2021). Metabolic regulation of neocortical expansion in development and evolution. *Neuron* **109**, 408-419. doi:10.1016/j.neuron.2020.11.014

Noctor, S. C., Flint, A. C., Weissman, T. A., Dammerman, R. S. and Kriegstein, A. R. (2001). Neurons derived from radial glial cells establish radial units in neocortex. *Nature* **409**, 714-720. doi:10.1038/35055553

Noctor, S. C., Martínez-Cerdeño, V., Ivic, L. and Kriegstein, A. R. (2004). Cortical neurons arise in symmetric and asymmetric division zones and migrate through specific phases. *Nat. Neurosci.* **7**, 136-144. doi:10.1038/nn1172

Paşca, S. P., Arlotta, P., Bateup, H. S., Camp, J. G., Cappello, S., Gage, F. H., Knoblich, J. A., Kriegstein, A. R., Lancaster, M. A., Ming, G.-L. et al. (2022). A nomenclature consensus for nervous system organoids and assembloids. *Nature* **609**, 907-910. doi:10.1038/s41586-022-05219-6

Pebworth, M.-P., Ross, J., Andrews, M., Bhaduri, A. and Kriegstein, A. R. (2021). Human intermediate progenitor diversity during cortical development. *Proc. Natl. Acad. Sci. USA* **118**, e2019415118. doi:10.1073/pnas.2019415118

Quinlan, A. R. and Hall, I. M. (2010). BEDTools: a flexible suite of utilities for comparing genomic features. *Bioinformatics* **26**, 841-842. doi:10.1093/bioinformatics/btq033

Rakic, P. (1972). Mode of cell migration to the superficial layers of fetal monkey neocortex. *J. Comp. Neurol.* **145**, 61-83. doi:10.1002/cne.901450105

Roussat, M., Jungas, T., Audouard, C., Omerani, S., Medevielle, F., Agius, E., Davy, A., Pituello, F. and Bel-Vialar, S. (2023). Control of G2 phase duration by CDC25B modulates the switch from direct to indirect neurogenesis in the neocortex. *J. Neurosci. Off. J. Soc. Neurosci.* **43**, 1154-1165. doi:10.1523/JNEUROSCI.0825-22.2022

Serrano, M., Pérez-Dueñas, B., Montoya, J., Ormazabal, A. and Artuch, R. (2012). Genetic causes of cerebral folate deficiency: clinical, biochemical and therapeutic aspects. *Drug Discov. Today* **17**, 1299-1306. doi:10.1016/j.drudis.2012.07.008

Sessa, A., Mao, C. A., Hadjantonakis, A.-K., Klein, W. H. and Broccoli, V. (2008). Tbr2 directs conversion of radial glia into basal precursors and guides neuronal amplification by indirect neurogenesis in the developing neocortex. *Neuron* **60**, 56-69. doi:10.1016/j.neuron.2008.09.028

Shiraki, N., Shiraki, Y., Tsuyama, T., Obata, F., Miura, M., Nagae, G., Aburatani, H., Kume, K., Endo, F. and Kume, S. (2014). Methionine metabolism regulates maintenance and differentiation of human pluripotent stem cells. *Cell Metab.* **19**, 780-794. doi:10.1016/j.cmet.2014.03.017

Shyh-Chang, N., Locasale, J. W., Lyssiotis, C. A., Zheng, Y., Teo, R. Y., Ratanasirintrawoot, S., Zhang, J., Onder, T., Unternaehrer, J. J., Zhu, H. et al. (2013). Influence of threonine metabolism on S-adenosylmethionine and histone methylation. *Science* **339**, 222-226. doi:10.1126/science.1226603

Telley, L., Agirman, G., Prados, J., Amberg, N., Fièvre, S., Oberst, P., Bartolini, G., Vitali, I., Cadilhac, C., Hippenmeyer, S. et al. (2019). Temporal patterning of apical progenitors and their daughter neurons in the developing neocortex. *Science* **364**, eaav2522. doi:10.1126/science.aav2522

Thoms, J. A. I., Knezevic, K., Liu, J. J., Glaros, E. N., Thai, T., Qiao, Q., Campbell, H., Packham, D., Huang, Y., Papathanasiou, P. et al. (2016). Arrested hematopoiesis and vascular relaxation defects in mice with a mutation in Dhfr. *Mol. Cell. Biol.* **36**, 1222-1236. doi:10.1128/MCB.01035-15

Trevino, A. E., Müller, F., Andersen, J., Sundaram, L., Kathiria, A., Shcherbina, A., Farh, K., Chang, H. Y., Paşca, A. M., Kundaje, A. et al. (2021). Chromatin and gene-regulatory dynamics of the developing human cerebral cortex at single-cell resolution. *Cell* **184**, 5053-5069.e23. doi:10.1016/j.cell.2021.07.039

Van Galen, P., Viny, A. D., Ram, O., Ryan, R. J. H., Cotton, M. J., Donohue, L., Sievers, C., Drier, Y., Liau, B. B., Gillespie, S. M. et al. (2016). A multiplexed system for quantitative comparisons of chromatin landscapes. *Mol. Cell* **61**, 170-180. doi:10.1016/j.molcel.2015.11.003

Vasistha, N. A., Garcia-Moreno, F., Arora, S., Cheung, A. F. P., Arnold, S. J., Robertson, E. J. and Molnar, Z. (2015). Cortical and clonal contribution of Tbr2 expressing progenitors in the developing mouse brain. *Cereb. Cortex* **25**, 3290-3302. doi:10.1093/cercor/bhu125

Villalba, A., Götz, M. and Borrell, V. (2021). Chapter One - The regulation of cortical neurogenesis. In *Current Topics in Developmental Biology* (ed. G. J. Bashaw), pp. 1-66. Academic Press.

Visel, A., Thaller, C. and Eichele, G. (2004). GenePaint.org: an atlas of gene expression patterns in the mouse embryo. *Nucleic Acids Res.* **32**, D552-D556. doi:10.1093/nar/gkh029

Zhang, Y., Liu, T., Meyer, C. A., Eeckhoute, J., Johnson, D. S., Bernstein, B. E., Nusbaum, C., Myers, R. M., Brown, M., Li, W. et al. (2008). Model-based analysis of ChIP-Seq (MACS). *Genome Biol.* **9**, R137. doi:10.1186/gb-2008-9-9-r137